ACTUATORS

Tactile displays driven by projected light

Max Linnander[1], **Dustin Goetz**[1]†, **Gregory Reardon**[2]‡, **Vijay Kumar**[1], **Elliot Hawkes**[1], **Yon Visell**[1,2,3,4]*

Tactile displays that lend tangible form to digital content could transform computing interactions. However, achieving the resolution, speed, and dynamic range needed for perceptual fidelity remains challenging. We present a dynamic tactile display that directly converts projected light into visible and tactile patterns via a photomechanical surface populated with millimeter-scale optotactile pixels. The pixels transduce incident light into mechanical displacements through photostimulated thermal gas expansion, yielding millimeter-scale displacements with response times of 2 to 100 milliseconds. The use of projected light for power transmission and addressing renders these displays highly scalable. We demonstrate optically driven displays with up to 1511 addressable pixels, several times more pixels than prior tactile displays attaining comparable performance. Perceptual studies confirm that these displays can reproduce diverse spatiotemporal tactile patterns with high fidelity. This research establishes a foundation for practical and versatile high-resolution tactile displays driven by light.

INTRODUCTION

Dynamic tactile displays are emerging technologies that render digital information in physical form, enabling users to touch, feel, and interact with digital content. These displays leverage arrays of individually addressable surface elements, or "tactile pixels" analogous to pixels in video displays, to represent spatial structure, temporal variation, and motion. Dynamic tactile displays might be used to present interactive controls, real-time data representations, virtual objects, or physical simulations, among other possibilities. Similar to digital video displays, whose emergence in the 20th century transformed computing, dynamic tactile displays are not designed for a specific application. Instead, they provide a general-purpose interface for rendering digital content in perceivable physical form. As with early visual display technologies, the most notable applications are difficult to predict in advance. Potential uses span many domains, including automotive interfaces emulating physical controls (*1*–*3*), interactive wall surfaces (*4*–*6*), educational electronic books (*7*, *8*), and user interfaces for virtual and augmented reality (*9*, *10*).

For tactile displays to present dynamic spatial content with perceptual fidelity, they must be able to render tactile patterns that are perceptually coherent in space and time. For example, short refresh intervals ($\leq$50 ms) are needed to maintain perceptual continuity across actuation cycles (*11*, *12*), similar to frame rate requirements for persistence of vision in video displays. Adequate spatial resolution ($\leq$3 mm) and dynamic range of displacement ($\gtrsim$1 mm) and force ($\gtrsim$ 5 mN) with proportional output are also needed (*11*, *13*–*15*). Sufficient display area is needed (and enough pixels) so that displays can present content anywhere on their surface for the intended application configuration. Achieving these requirements in displays of useful sizes at sustainable costs may require substantial advancements in actuation technologies, scalability, integration density, and fabrication methods.

A variety of materials and actuation methods have been studied for dynamic tactile display engineering, including electrostatic, piezoelectric, electromagnetic, fluidic, and electroosmotic methods (*16*–*22*). However, the state of the art remains dominated by bespoke displays with a hundred or fewer pixels; see table S1 and a survey (*22*). Braille displays, a distinct class of pin-array devices, present tactile graphics for several seconds to allow manual exploration and interpretation (*23*). Thus, they are not normally designed to operate at the refresh rates ($\geq$20 Hz) required for dynamic tactile displays to maintain perceptual continuity. Although it is feasible to realize dynamic devices with many addressable elements, scaling electronic tactile displays to larger sizes and resolutions at sustainable cost and complexity remains a challenge. As size and resolution increase, the complexity of driving and control circuits grows rapidly. Moreover, modifying the configuration of such systems often requires electronic redesign, hindering development.

An intriguing alternative is to exploit light transmission for tactile actuation. Tactile displays are often designed to integrate with video displays that use optical transmission. Harnessing light for tactile actuation presents a synergistic opportunity that could offer practical and performance benefits. Optical energy can be modulated at high frequencies and directed with high spatial precision using mature technologies, including video and laser projection, enabling rapid and localized wireless energy delivery. Even compact laser modules can deliver substantial power via light (~5 W), as much as would be required to drive dozens of miniature vibration actuators (*24*, *25*). The use of projected light for tactile displays may simplify power distribution and control, reducing system complexity and supporting scalability.

Despite its potential, targeted light transmission for tactile actuation has been sparsely investigated. Prior studies have used thermal mechanisms for photomechanical transduction by converting absorbed light into heat, which was then transformed into tactile actuation. Examples include solid thermoelastic expansion (*26*), phase transitions in liquid crystal elastomers (*27*, *28*), and liquid vaporization (*29*). In part, because of constraints arising from heat transfer, these systems have often exhibited slow response times of seconds or longer (table S2). Using a captive gas as the working medium can enable tactile displays to achieve the rapid response times that are required for perceptual fidelity. Gases exhibit high thermal diffusivity,

---

[1]Department of Mechanical Engineering, University of California, Santa Barbara, CA, USA. [2]Media Arts and Technology Program, University of California, Santa Barbara, CA, USA. [3]Department of Bioengineering, University of California, Santa Barbara, CA, USA. [4]Department of Electrical and Computer Engineering, University of California, Santa Barbara, CA, USA.
*Corresponding author. Email: yonvisell@ucsb.edu
†Present address: Apple Inc., Cupertino, CA, USA.
‡Present address: Northwestern University, Evanston, IL, USA.

α, because of their low density. High diffusivity promotes rapid heat transfer because the heat transfer timescale, τ, is inversely proportional to α. The low density of gases facilitates high temperatures, because the addition of heat, Q, yields a temperature increase that is inversely proportional to density. Larger temperatures result in faster thermal responses because heat is transferred out of the actuator at a rate that is proportional to the difference in temperature, ΔT, consistent with Newton's law of cooling.

Directly heating a captive gas with light is challenging, because gases are generally transparent. However, efficient heat transfer to a gas can be achieved by integrating a low–thermal mass photoabsorber within a gas-filled cavity. Such a configuration may enable rapid actuation cycles suitable for tactile displays driven by projected light. This principle has historical parallels in experiments by Bell, Tyndall, and Röntgen in the 1880s, where intermittent illumination of absorbing materials in gas-filled cavities was observed to yield audible sound (*30*–*32*). Similar principles have been exploited in prior research on remote power transmission for aerospace (*33*), thermodynamic actuation (*34*), optically driven micromechanical valves (*35*–*37*), and photoacoustic spectrometry (*38*), among other systems.

Building on these insights, we present a tactile display that uses projected light to activate tactile patterns across a surface populated with small optotactile pixels (characteristic dimension L = 3 mm). Each pixel contains a thin-film photoabsorber suspended in a captive gas. Photostimulation of a pixel drives rapid heating, inducing transient gas expansion (Fig. 1). Light pulses with energies of 2.5 to 125 mJ are sufficient to activate localized displacements and forces. Pixel response times from 2 to 100 ms are feasible. We demonstrate devices that achieve pixel displacements of 1 mm and forces of 55 mN, after 50 ms of photostimulation at optical power P_L = 2.5 W. The actuation method, optical addressing technique, and simplicity of fabrication make this technique practical and scalable. We present implementations with up to 1511 independently addressable pixels distributed over a 15 cm–by–15 cm area, several times more pixels than previous tactile displays approximating the requirements cited above (Fig. 1I and table S1). We show that these light-driven tactile displays are capable of representing a wide variety of spatiotemporal tactile patterns that can be accurately perceived.

RESULTS

Design and photomechanical transduction principle

The display reproduced visible, tactile patterns by translating projected light into mechanical signals, using an array of optically addressed pixels (Fig. 1, A and B). Each pixel operated on a thermodynamic principle, transducing optical energy into heat and heat into work. Light entering the pixel was converted to heat by a thin photoabsorber suspended in a captive gas (Fig. 1C). The absorber rapidly increased in temperature, transferring heat to the gas, which thus led to a pressure increase dictated by the ideal gas law. Gas expansion drove the deflection of an elastic tactile membrane sealing the pixels, yielding localized mechanical forces $F(t)$ and displacements $z(t)$ that could be felt by touching the membrane (Fig. 1D).

This general strategy may be used to realize a large variety of displays. The following design choices exemplify one way that it can be implemented. A multilayered architecture was used to facilitate ease of manufacturing and scalability (Fig. 1B). Transparent acrylic formed a base layer, functioning as the optical window (fig. S2). An array of cylindrical pixel cavities was formed from two polysiloxane (PS) layers that were patterned via laser cutting (Fig. 1C and figs. S4 and S5). The pixel dimensions (diameter of 3 mm and height of 1 mm) were selected on the basis of perceptual requirements, theoretical analysis, and numerical simulations (see Supplementary Methods). A pyrolytic graphite sheet (PGS; 18 μm) was positioned between the pixel cavity layers and patterned to form an array of photoabsorbers suspended by narrow bridge features (Fig. 1, C and D, and fig. S4). PGS was selected because of its high thermal conductivity, broad spectrum photoabsorption (fig. S2), and thermal stability. Capping this assembly was the tactile membrane, an elastomer that sealed the air-filled cavities. The display could be made flexible through the use of a thinner or more elastic transparent base layer (Fig. 1G).

The pixels were stimulated by brief low-energy light pulses (2.5 to 125 mJ) delivered from a compact diode laser [wavelength (λ) = 450 nm; Fig. 1C and fig. S6]. Optical addressing was facilitated by commodity *xy* scanning galvanometer mirrors, yielding spatiotemporal tactile patterns that could be felt and also seen (movies S1 to S3). The patterns were made visible through the transmission of light scattered through the membrane at each pixel (Fig. 1, E and F). The mechanism of actuation, optical powering, and addressing technique; simplicity of fabrication; and use of widely available materials render this technology practical and scalable (tables S4 and S5). To demonstrate the ease of manufacturing and scalability, we fabricated devices with 1, 16, 357, and 1511 addressable pixels (Fig. 1H) using the same fabrication methods for each. In these devices, the linear pixel pitch was 4 mm, including the spacing between pixels; thus, each pixel occupied a net surface area A_p = 0.16 cm^2. Our results indicate that the devices achieve forces, displacements, resolutions, and response rates meeting perceptual requirements for dynamic tactile display at display scales suitable for diverse applications (Fig. 1I, fig. S15, and table S1).

Thermomechanical response under photostimulation

We experimentally characterized the thermal and mechanical response of individual pixels driven by discrete light pulses with duration t_p = 50 ms and power P_L. We observed that the mean temperature $T(t)$ in the photoabsorber rises monotonically during exposure (Fig. 2, A to D), driving expansion of air within the pixel cavity and deflection of the tactile membrane (movie S4). Temperature and displacement both reached their maximum values near the time at which the optical pulse ceased, indicating a nearly static relationship between the absorber and air temperatures during heating (Fig. 2D and fig. S8). After the pulse, temperature and displacement relaxed toward baseline conditions.

The timescale for the pixel displacement to relax to baseline was governed by heat transfer. The thermal and mechanical response characteristics of the pixel could be tuned by adjusting the photoabsorber geometry. We studied the effect of varying the width, w, of the bridges suspending the photoabsorber in the cavity, from w = 0.2 to 0.75 mm (Fig. 2, A to D, and movie S5). Larger $T(t)$ values and displacements, $z(t)$, were obtained from pixels with smaller w, indicating that bridge width has a dominant effect on heat transfer out of the pixel. We confirmed this using theoretical and numerical analyses of heat transfer (see Supplementary Methods). The highest absorber temperatures and displacements were obtained at the smallest width, w = 0.2 mm. Temperature increased by 507°C, and displacement reached a maximum of 0.97 mm after 50 ms of photostimulation at 2.5 W (movie S6).

A thermal resistance parameter, R, encoded the influence of w on heat transfer and could be adjusted to tune pixel response time or

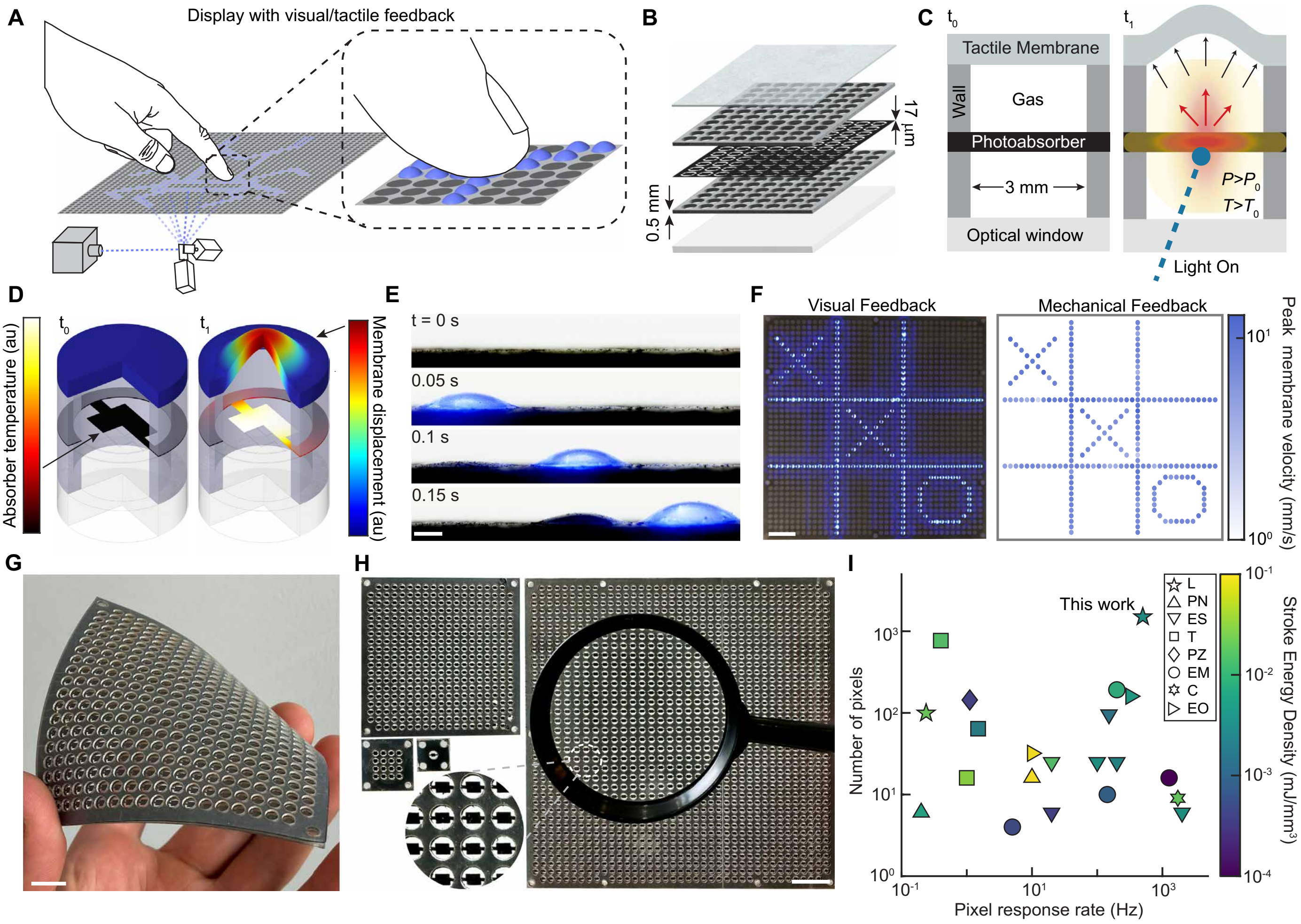

Fig. 1. Tactile display driven by projected light. (**A**) The display directly converts projected light into visible, tactile patterns via an array of optotactile pixels. (**B**) Light is converted to forces and displacements via an assembly of patterned layers, supporting manufacturing and scalability. Layers: tactile membrane (EcoFlex 00-10), cavity walls (PS), thin photoabsorber (PGS; thickness, 18 µm), cavity walls (PS), and optically transparent window (acrylic). (**C**) Pixel operation (section view). An incident light pulse is converted into heat by the photoabsorber. Heat is transferred to air in the cavity, raising gas temperature T and pressure P. Gas expansion drives the deflection of the elastic membrane. (**D**) FEA of pixel thermomechanical response. au, arbitrary units. (**E**) Sequential photostimulation of pixel arrays elicits both visual feedback, because of the transmission of scattered light through the membrane, and tactile feedback, because of the mechanical deflection of the tactile membrane. Scale bar, 1 mm. (**F**) Extended exposure (2.12 s) image of 1511-pixel display with corresponding membrane velocity. Scale bar, 2 cm. (**G**) Flexible tactile display with tactile membrane removed for visual purposes, 357 pixels. Scale bar, 1 cm. (**H**) This technique can be used to realize displays that vary in dimensions and pixel count. We show displays with 1, 8, 357, and 1511 pixels (tactile membrane removed for visual purposes). Scale bar, 2 cm. (**I**) Comparison with prior tactile displays. Our display enables rapid response rates, scales to pixel counts surpassing prior work, and is uniquely capable of both visual and tactile display. Driving mechanisms: L, light; EM, electromagnetic; PN, pneumatic; ES, electrostatic, T, thermal; PZ, piezoelectric; C, combustion; and EO, electroosmosis. See the Supplementary Materials for additional information.

displacement. We identified R by analyzing the experimental data in tandem with an effective description of heat transfer. The timescale τ governing the absorber temperature response, $T(t)$, to photostimulation is given by

$$\tau = RC \tag{1}$$

where C is the absorber heat capacity. After photostimulation ceased, the pixel relaxed to its initial state over a timescale approximately given by τ. Values for R and C were obtained by numerical fit to experimental data (table S2). R was inversely proportional to w, in agreement with the theoretically expected relationship

$$R = \frac{L}{k_{xy} h w} \tag{2}$$

where k_{xy} is the in-plane thermal conductivity of the PGS absorber, h is thickness, and L is the characteristic length scale of the device, over which heat is transferred. The data agreed with the predicted inverse relationship with a coefficient of determination (r^2) of 0.98 (Fig. 2E). By adjusting R, we could tune τ in the range 10 ms $\leq \tau \leq$ 100 ms. Selecting larger values of R yielded larger peak displacements and longer τ (Fig. 2F). These competing effects illustrate a trade-off between response amplitude and response speed that we examined in experiments detailed in the next section. The values of R that were selected were chosen to highlight salient aspects of the display gamut of these devices.

When the t_p exciting a pixel was shorter than τ, the period over which the pixel relaxed was longer than the excitation period, as can

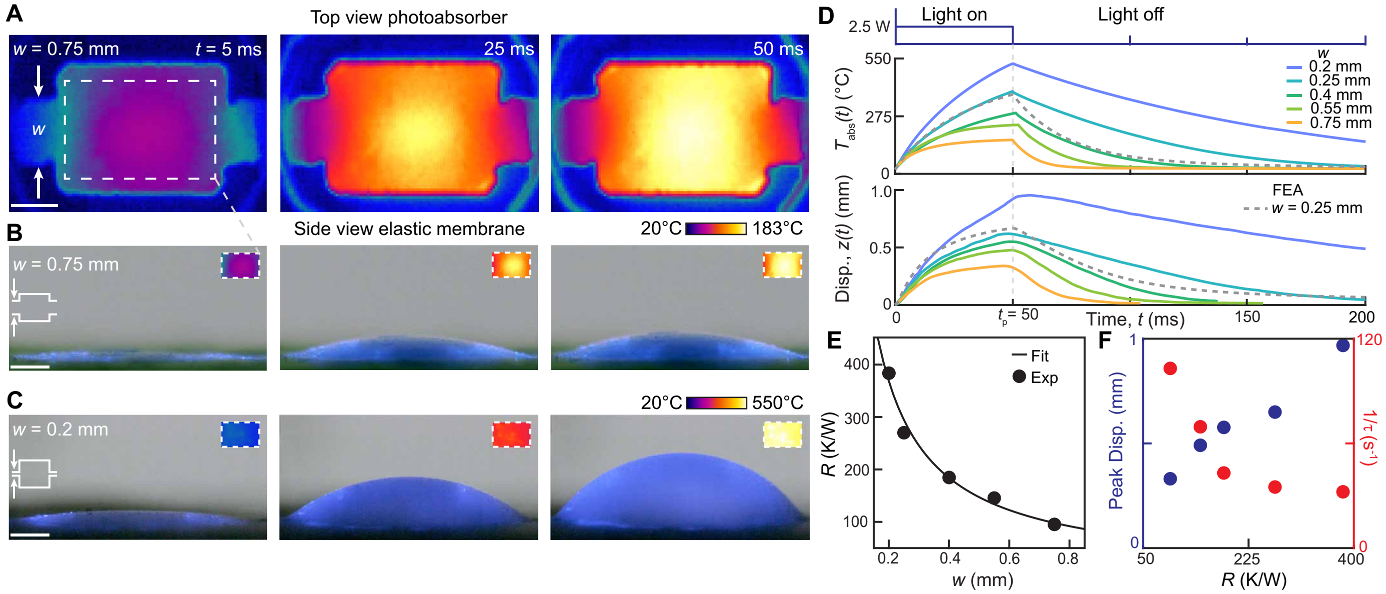

Fig. 2. Thermal-mechanical response under photostimulation. (**A** and **B**) Absorber surface temperature and membrane deflection increased monotonically during illumination with $P_L = 2.5$ W over 50 ms. Scale bar, 0.5 mm. (**C**) Reducing the thermal bridge width from $w = 0.75$ mm to 0.2 mm yielded higher temperatures and larger displacements. Scale bar, 0.5 mm. (**D**) Experimental $T(t)$ and membrane displacement $z(t)$ versus time t for $w = 0.2$, 0.25, 0.4, 0.55, and 0.75 mm. As w decreased, more heat was retained in the absorber, yielding higher temperatures and larger displacements. Gray dashed line: numerical results for $w = 0.25$ mm. (**E**) The thermal resistance R of the bridge increased as w decreased. Black line, reciprocal fit: $R = a/w$ with $a = 73.3$ mm K/W, $r^2 = 0.98$. (**F**) Peak membrane displacement and absorber thermal relaxation time τ increased with thermal bridge resistance R, whereas the relaxation rate $1/\tau$ decreased, indicating that tuning w involves a trade-off between displacement and relaxation rate.

be seen in Fig. 2D. However, in such conditions, sensation typically aligns with the shorter excitation period. This is because many tactile receptors in the skin, including numerous Meissner corpuscles, are rapidly adapting and thus most sensitive to temporal changes in skin deformation and because the skin recovers from deformation with substantial latency because of its intrinsic viscoelasticity (*14*).

Rapid refresh of photostimulated tactile pixels

Achieving rapid pixel responses is essential for enabling dynamic tactile displays to render content that is perceptually coherent in time, across refresh cycles (*11*, *12*), similar to frame rate requirements for persistence of vision in visual displays. Rapid pixel responses also enhance the bandwidth of information conveyance, increase display responsiveness, and support perceptual fidelity by engaging the dense populations of fast-adapting mechanoreceptors in glabrous skin (*14*). Our display exhibited rapid actuation cycles, from 2 to 100 ms, that contrast with slower response times, 1 s or more, that are often obtained with thermally mediated actuation (fig. S15). This performance was enabled by the high thermal diffusivity of the captive gas and the low thermal mass of the photoabsorber (100 μJ/K) and gas (10 μJ/K), by the small quantity of heat energy delivered in each pulse (2.5 to 125 mJ), and by favorable heat transfer characteristics, including the surface area–to–volume ratio, $A/V \propto 1/L$, where $L = 3$ mm.

However, achieving rapid actuation cycles in tactile displays is balanced by the competing need for sufficient dynamic range in force and displacement. In our system, this trade-off was parametrized by the effective R value of the absorber. To evaluate this balance, we experimentally characterized the membrane force and displacement responses across a range of optical stimuli (Fig. 3). We observed the peak output force to increase linearly with increasing P_L (Fig. 3B). At constant power, force and displacement increased monotonically with t_p (Fig. 3B and fig. S7). With pulse duration held constant, we measured the largest forces ($F = 55$ mN for $t_p = 50$ ms) at the highest resistance ($R = 382$ K/W) and smaller forces ($F = 31$ mN) at lower resistance ($R = 145$ K/W; Fig. 3B and fig. S9).

Using these measurements, we computed the stroke efficiency, η_s, of actuation as the ratio of stroke power, P_s, to absorbed P_L, εP_L, and obtained $\eta_s = 0.03\%$ (fig. S11). This efficiency is within the range observed for many thermal actuation methods (table S1). It reflects several losses. More than 90% was due to heat transfer from the photoabsorber to the walls via the bridges. This thermal conduit facilitated rapid pixel responses at the expense of efficiency and dynamic range. By adjusting R, we could tune this balance. The energetic conversion of heat in the gas into output work was about 14% efficient. The loss represents entropy generation (*39*), a measure of irreversibility, and is magnified at small scales. In our device, V was equal to 7.8 μl. A general scaling analysis indicates that when the L of a thermally actuated device is sufficiently small, the loss in efficiency scales as $L^{-\alpha}$, where $\alpha = 1$ or 2 depending on the heat input configuration. Similar size-efficiency effects have been experimentally observed across many thermodynamic systems (*40*, *41*). For additional information about energetic performance and the scaling analysis, see Supplementary Methods.

We next investigated temporal parameters governing the dynamic response of the display under cyclic photostimulation. Rapid stimulation produced a multimodal displacement response with slowly varying and oscillating components, $d(t)$ and $\delta(t)$, respectively (Fig. 3C). The slow component, $d(t)$, was due to the retention of heat in the cavity across cycles, as occurred when the interpulse

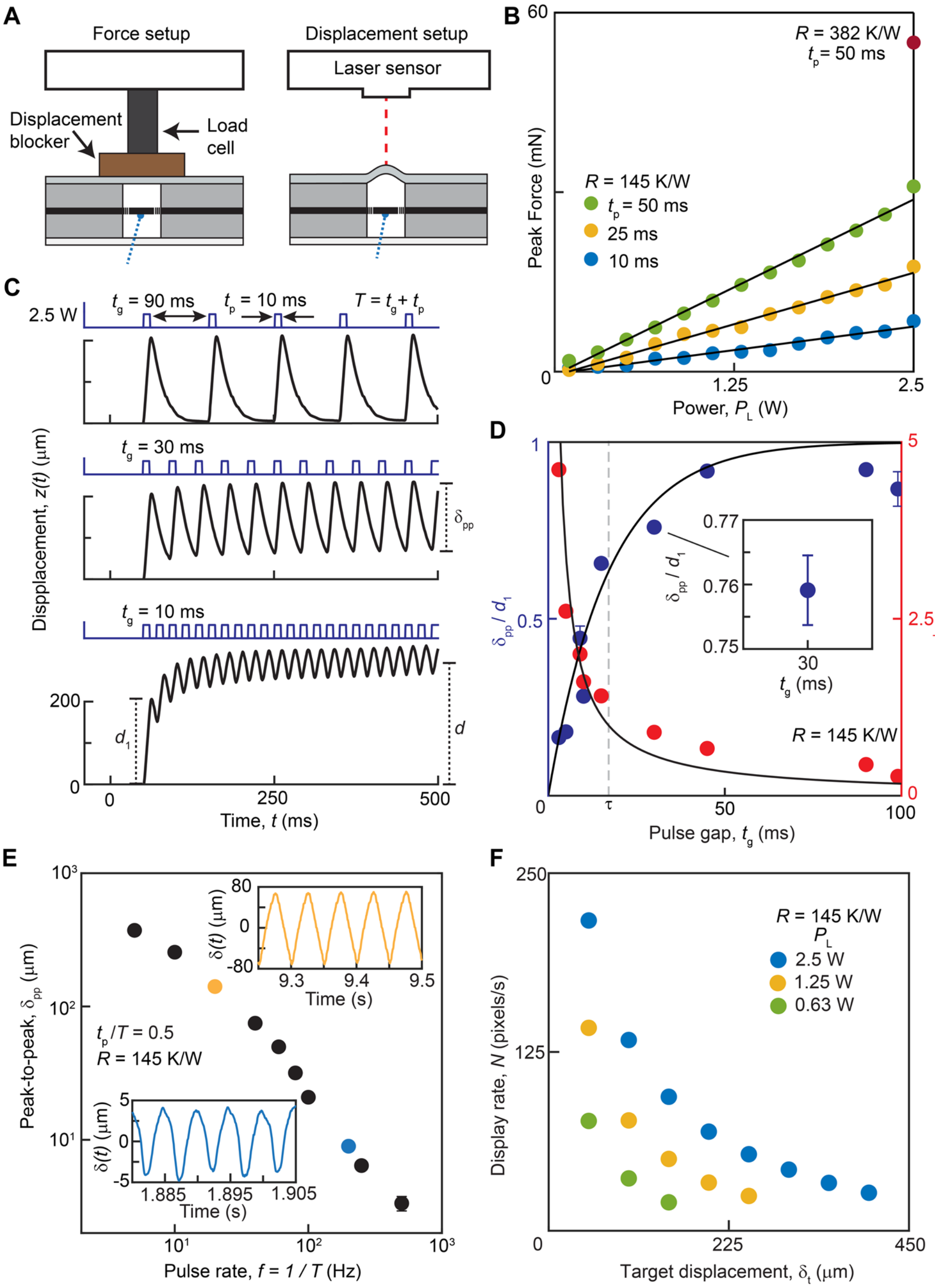

Fig. 3. Cyclic photostimulated actuation. (**A**) Isometric force and unloaded displacement measurements. (**B**) Force increased linearly with P_L and increased with t_p, with a measured peak of $F = 55$ mN. Black solid lines denote linear regression fits. (**C**) Successive displacement responses to pulsed excitation exhibit minimal variation for $t_g \gg \tau$, where $\tau \approx 17$ ms and $R = 145$ K/W. At shorter t_g, heat accumulates, yielding a slowly varying component, $d(t)$, and a reduction in δ_{pp} relative to the first pulse amplitude, d_1. (**D**) As t_g increases, δ_{pp} (blue circles) increased. The analytic model, $\delta_{pp}/d_1 = 1 - \exp(-t_g/\tau)$ ($r^2 = 0.92$), captures this trend. The magnitude, d, of the slow component (red circles) followed an opposite trend, consistent with the model $d/d_1 = \tau/t_g$ ($r^2 = 0.86$). Black lines show model predictions evaluated with the experimental value of $\tau = 17$ ms (uncertainty bars: 1 SD, $n = 5$). (**E**) Displacements δ_{pp} for pulse frequencies $f = 5$ to 500 Hz. Peak-to-peak displacement decreased as f increased, with $t_p/t_g = 1$. Insets: Oscillating component, $\delta(t)$ for $f = 20$ Hz (yellow line) and 200 Hz (blue line). (**F**) In sequential scanning, N is dictated by the target displacement, d. At fixed P_L, N decreases as displacement increases. For $P_L = 2.5$ W, $N = 217$ pixels/s is achieved at 50 μm, and $N = 26.5$ pixels/s is achieved at 400 μm.

gap time, t_g, was shorter than τ. In steady state, the amplitude of $d(t)$ decreased as t_g increased (Fig. 3D, red circles). The peak-to-peak amplitude, δ_{pp}, of the oscillating component exhibited an opposite trend (Fig. 3D, blue circles). Across a range of values of t_g, both components fall within the perceptually notable amplitude range (*14*). Thus, by adjusting t_g, we can control the relative proportion of slow and vibratory tactile feedback.

Altering the pulse rate, f, differentially modulated the amplitude of the two components of displacement. At constant power and duty cycle t_p/T, the amplitude of $d(t)$ was nearly invariant with respect to variations in f (fig. S10). This occurred because the time-averaged absorbed power, $\overline{P}$, is proportional to t_p/T and to P_L. In contrast, because t_p and t_g both decreased as f increased, δ_{pp} decreased (Fig. 3E). Nonetheless, even rapid pulsing at $f = 200$ Hz yielded $\delta_{pp} = 8.4$ μm, which is sufficient to be perceived via touch. For comparison, this amplitude is about 25 dB higher than the perceptual detection threshold for 200-Hz vibrations at the fingertip (*42*).

Although the response rate of individual pixels was constrained by τ, our display could render tactile patterns by rapidly scanning the light source across arrays of pixels in sequence (movies S2 and S3). In this mode of operation, the excitation phase of one pixel overlapped with the relaxation phase of the preceding pixel. The extent of this overlap was determined by τ, which depends on R. As expected from our theoretical and numerical studies, adjacent pixels in our prototype displays exhibited negligible fluidic or thermal crosstalk, as can be observed by comparing the first two time instants of the imaging data shown in Fig. 1E or fig. S21.

In sequential scanning, the maximum display rate, N, in pixels per second, was dictated by the t_p needed to achieve a specified target displacement, δ_t, at operating P_L. N thus decreased with increasing displacement (Fig. 3F). Using our experimental results for a pixel with $R = 145$ K/W at $P_L = 2.5$ W (Fig. 2D), for $\delta_t = 50$ μm, we obtained N of 217 pixels/s. For $\delta_t = 400$ μm, N was equal to 26.5 pixels/s. Higher rates can be achieved by increasing optical power or by using multiple optical sources in parallel. With K optical sources, the display rate would be proportionally higher.

Tactile pattern display and perception

This tactile display used a physical operating principle that diverged from those used in prior haptic technologies. The forces and displacements that were produced by individual pixels (up to 55 mN and 0.97 mm) were well within the perceivable range (*14*). These basic capabilities led us to investigate the potential of using multiple pixels to render a variety of perceptually distinct tactile patterns. We conducted six experiments assessing the perception of linear and rotational motion patterns, tactile localization, the scaling of perceived intensity with power, the perception of temporal patterns, and multifinger tactile perception (Fig. 4, A to F). The same 10 participants completed all six experiments without training.

Experiment 1 assessed the perception of linear motion patterns that were generated through the sequential activation of pixels along each of four cardinal directions (Fig. 4A and movie S2). All participants correctly reported the motion direction in 100% of trials. In experiment 2, participants discriminated rotational motion patterns at three different motion speeds (Fig. 4B). Their response accuracy was 94.6%. These results underscore the effectiveness of the display in representing motion.

In experiment 3, participants reported which single pixel was actuated out of nine pixels arranged in a 1 cm–by–1 cm grid beneath the finger pad (Fig. 4C). They responded correctly in 78.4% of trials. The mean error in localization was 0.17 mm, with 99% of all responses within 1 pixel of the correct location. As a point of comparison, the two-point discrimination threshold, a standard measure of tactile acuity, averages 2 to 3 mm at the fingertip (*43*).

In experiment 4, we assessed the relationship between perceived intensity and optical power (Fig. 4D) using the psychophysical method of magnitude estimation. Participants rated the intensity of impulse trains that were excited at different power levels (0.5 to 2.5 W). Perceived intensity increased linearly with optical power ($r^2 = 0.98$) and thus increased linearly with force (Fig. 3B). Thus, perceptually distinct levels of tactile feedback could be generated by modulating power.

In experiment 5, participants discriminated temporal patterns (Fig. 4E) using an odd-one-out paradigm. In each trial, they felt a

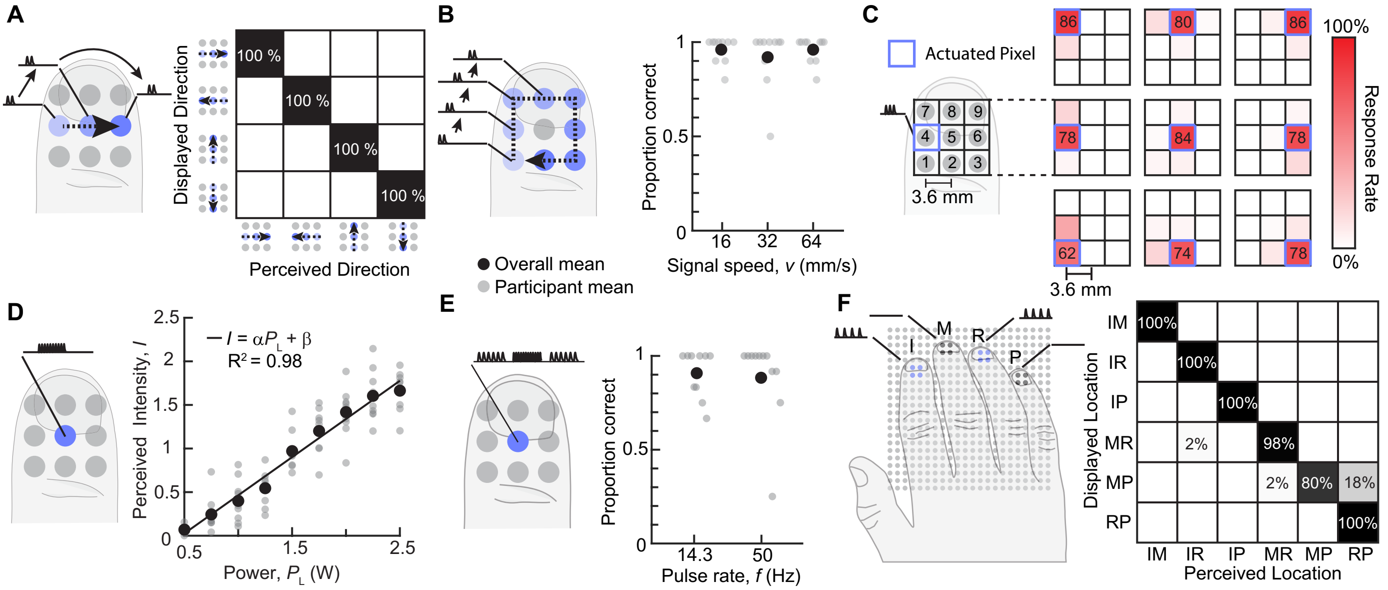

Fig. 4. Perception of dynamic tactile pattern display. (**A**) Experiment 1: perception of linear tactile motion patterns. (**B**) Experiment 2: perception of rotational motion for motion speeds $v = 16$, 32, and 64 mm/s. Black dots show the overall mean, and gray dots show participant mean. (**C**) Experiment 3: spatial localization of actuated pixels on the finger pad. (**D**) Experiment 4: the perceived intensity of pulse train feedback from a single pixel increased linearly with P_L. Regression fit: $\alpha = 0.022$, $\beta = -0.42$. (**E**) Experiment 5: discrimination of temporal patterns. Odd-one-out task to identify which of three sensations was different. (**F**) Experiment 6: perception of multipoint tactile patterns felt at any two of four fingers. All perceptual experiments were performed on a display with $R = 145$ K/W.

sequence of three temporal pulse train patterns generated at a single pixel. Two patterns had the same pulse rate, either slow or fast (14.3 or 50 Hz), whereas the third stimulus, the oddball, had a different pulse rate (respectively, fast or slow). These temporal patterns exploited the multimodal capability of our display; the 14.3- and 50-Hz pulse trains produced both oscillating and slow components with respective amplitude ratios of $\delta_{pp}/d = 1.2$ and $\delta_{pp}/d = 0.15$ (Fig. 3D). Participants correctly discriminated the temporal patterns, identifying the oddball stimulus, in 89.6% of all trials.

In experiment 6, we investigated the perception of multipoint tactile pattern perception. In each trial, participants simultaneously felt stimuli on two of four fingers in contact with the display and reported the pair of stimulated locations. Participants correctly identified the pair of locations with 96.3% accuracy.

In postexperiment surveys, no participant reported seeing any optical stimuli or perceiving thermal sensations. Further measurements revealed that the experimental stimuli induced small surface temperature increases on the membrane, ΔT_{surf}, on the order of 1°C (fig. S18). This was expected given that an air gap impedes heat transfer from the photoabsorber to the touched surface, consistent with our theoretical and numerical analyses (see Supplementary Methods). For comparison, contact by a human finger raised the surface temperature by 4°C after 10 s (fig. S18).

CONCLUSION

Our tactile display technique exploits the advantages of projected light for power transmission, addressing, and actuation. Light is directly transduced into forces and displacements via energetically passive surfaces populated with optotactile pixels. The actuation mechanism, layered architecture, and simplicity of fabrication make it straightforward to produce displays with dozens to thousands of pixels, with similar investments in material cost and fabrication time. We present implementations with up to 1511 pixels, substantially more than previous devices capable of similar performance, notably in response time and amplitude. Our technique furthermore yields tactile patterns that can be not only felt but also seen, enabling multisensory tactile displays. These displays hold promise for applications ranging from automotive interfaces to virtual reality controllers. Higher pixel display rates than those attained by our prototypes may facilitate the adoption of such displays in more areas. They could be achieved using optimized architectures that exploit fundamental knowledge about thermodynamic device efficiency and by leveraging high-power optical projection technologies like those being developed for additive manufacturing and automotive applications (*44*). The optical system used in this research was sufficient for prototyping but could be miniaturized through the use of optical waveguides or fiber optic coupling. These improvements could enable widespread deployment of high-definition projected light tactile displays that lend physical form to otherwise intangible digital data. The future influence of such displays is, however, difficult to predict today. One can draw an analogy to the development of digital video displays in the middle of the 20th century. Although early visual displays enabled the emergence of desktop computing, their commercialization also catalyzed new industries, such as video games, that were largely unanticipated. Emerging tactile displays could, likewise, have a substantial effect on the future of human-computer interaction.

MATERIALS AND METHODS

Display fabrication

The same manufacturing steps were used for displays with 1 to 1511 pixels. The display surface is a layered assembly. In order from base to top layer, the materials are transparent acrylic sheet, PGS (thickness of 18 μm), adhesive PS sheet, and cast silicone elastomer (thickness of 0.25 mm). Double-sided adhesive tape (2477, 3M, USA) was used to affix the lower PS sheet to the acrylic. The thickness of the acrylic may be selected on the basis of application requirements. For the flexible display, the thickness was 0.01 inches, and, for the rigid display, it was $^{1}/_{16}$ inches. Supplier information and representative costs for the materials are reported in table S4.

The PS sheets were patterned via laser cutting to form a grid of cylindrical cavities ($r_{\mathrm{cavity}} = 1.5$ mm, pitch = 4 mm; fig. S5). The PGS was patterned using a vinyl cutter to form a grid of rectangular photoabsorbers (2 mm by 1.5 mm) aligned with the cavities (fig. S5). The acrylic was laser-cut to form the square geometry; for the 1511 display, the dimensions are 162 mm by 162 mm (fig. S5). The PGS adhesive was dissolved via acetone processing and aligned between PS layers. For the cast elastomer, the two silicone elastomer component reagents were mixed, degassed, and placed into a mold with a depth of 250 μm. It was subsequently cured at room temperature for 24 hours. Because the resulting elastomer sheet was tacky, no adhesive was needed to affix it to the PS layer.

Photoabsorber thickness and density characterization

The thickness of the PGS photoabsorber was measured via profilometry and confocal microscopy. For the profilometer measurement (DektakXT, Bruker), the adhesive side of the PGS was applied to a glass slide. Measurements from four distinct samples of the combined thickness of PGS and adhesive were taken, yielding $h_{\mathrm{PGS,adh}} = 24.4$ μm (SD, ± 1.6 μm; fig. S16). We characterized the adhesive thickness using confocal microscopy (DSX1000, Olympus), obtaining $h_{\mathrm{adh}} = 6.5$ μm (instrument repeatability, ± 1 μm). Subtracting the two thicknesses yielded the PGS photoabsorber thickness, $h_{\mathrm{PGS}} = 17.9 \pm 2.6$ μm. The result was 7.9 μm larger than the thickness of 10 μm specified by the manufacturer. The mass of the PGS sample, after adhesive removal, was determined using a microbalance (XPR105, Mettler Toledo) to be 1.00 mg (SD, ± 0.06 mg, $n = 4$). The density was then computed via dimensional measurements of surface area (25 ± 5 mm^2, instrument resolution uncertainty) and thickness h_{PGS} (as noted above). This yielded a PGS density value of $\rho_{\mathrm{PGS}} = 2230 \pm 510$ kg/m^3, which is consistent with the manufacturer's specified value of 2130 kg/m^3. The PGS, thickness, mass, and density uncertainties were propagated analytically.

Optical stage

The optical stage included a two-axis galvo mirror system (Laserwinkel, Netherlands), a 4-W 450-nm diode laser (LT-20 W-A, Laser Tree), a collimating lens (Qiaoba), and an F-theta lens (Opex). The optical components were arranged in a three-dimensionally printed fixture. The laser path proceeded through the collimating lens, galvo, F-theta lens, and the optical window of the addressed pixel onto the respective photoabsorber (fig. S6). The optical stage was configured in an optically sealed enclosure with an aperture located at the top, where the display surface was positioned. Representative costs of components used to construct the optical stage are given in table S5.

The laser was powered with 12 V using a laboratory supply. Optical power output was modulated via pulse-width modulation (PWM frequency, 5 kHz) supplied to the laser by a data acquisition unit (NI SCB-68A) under computer control.

The maximum instantaneous optical power incident on the sample was 2.45 W, as measured via bolometer (S212A, Thorlabs, USA). This measured power accounted for transmission losses through the mirrors and lenses. Transmission through the acrylic layer was 92.4% at 450 nm (fig. S2), as determined by spectroscopic measurement (UV-1800 UV-VIS, Shimadzu, Japan). The optical absorption of the PGS at 450 nm was 72.3% (fig. S2). At maximum optical power, the power absorbed by the PGS was 1.63 W, accounting for all of the aforementioned losses. For angles of incidence in the range used here, the effect on optical transmission and photoabsorption is negligible.

Performance parameters specific to the optical stage used in this study are reported in table S6. The laser spot size was measured using the dimensions of the illuminated region on an optical target. The maximum scanning speed was 14.7 cm/ms, as experimentally determined from the greatest speed for which the beam could be driven to the extrema of the large display surface. The maximum feasible display dimensions depend on the optical system geometry and components. For those used here, the maximum width was 17 cm. The linear repeatability of the laser galvo mirrors was assessed by imaging the laser spot as it sequentially illuminated spatially separated locations on a target. The SD of the center of the laser spot was 13 μm along the x axis and 31 μm along the y axis.

Imaging

The PGS photoabsorber material and geometry were characterized using a microscope (AmScope, USA) and a laboratory scale with 50-μm divisions. We used a mid-wave infrared camera (Fast M3K, Telops, USA) and microscope lens (1×, Telops, USA) to collect the thermal data in Fig. 2. The camera was directed at the sample via a mid-infrared gold mirror (PFSQ20-03-M02, Thorlabs, USA) (fig. S14, A and B). The top elastomer sheet of the display was removed during thermal imaging. Time-resolved infrared videos were captured at a frame rate of 5000 fps using an exposure time of 5.04 μs and subsequently analyzed in RevealIR (Telops, USA), where an emissivity of 0.39 was used (fig. S3). Radiometric temperature calibration was performed separately for low and high temperature ranges, $T < 236°C$ and $T > 236°C$. Data captured across both ranges were combined in software (Fig. 2D) and aligned via temporal synchronization. For the sample with $w = 0.55$ mm, we performed model-based calibration to infer $T > 236°C$ (see Supplementary Methods).

Video data were captured using a high-speed camera (Phantom VEO 640 L, Vision Research, USA) with a microscope objective and a 2× Plan Apo infinity-corrected lens (WE1603, Mitutoyo, USA). The camera was directed at the profile of each sample (fig. S14, C and D). A measured sample (thickness of 2.2 mm) of cast acrylic was introduced into the field of view as a dimensional scaling reference. Optical imaging data were collected, reviewed, and saved in Phantom Video Player (Vision Research, USA). Metrology analysis was performed via manual annotation of points of interest using video analysis software (Tracker, version 6.1.5), yielding displacement values (Fig. 2, D to F).

An extended exposure photo, used for illustration in Fig. 1, was captured using the camera of an iPhone SE third generation via the app Spectre, with the "light trail" feature turned on. This image was not used for quantitative analysis.

Thermal resistance measurements

Values representing net R to heat transfer in and out of the absorber and C were obtained from experimental data by regression fit to the solution of a heat transfer equation (see Supplementary Methods), with $\tau = RC$. The fit was performed using temperature data acquired during the first 30 ms of photostimulation at 1.63 W. The temporal dependence of temperature, through $\tau = RC$, and the value of R obtained from the fit are generic and insensitive to modeling choices. The absorber was initially at room temperature during data collection. The experimentally determined C was equal to 100 μJ/K (SD, ±15 μJ/K, $n = 5$; table S2), which was in agreement with the value that we calculated on the basis of the geometry and properties of the photoabsorber, using $C = V_{abs}\rho_{abs}c_{abs} = 85$ μJ/K, where V_{abs}, ρ_{abs}, and c_{abs} are the volume, density, and specific heat capacity of the PGS optical target, respectively.

Numerical experiments

We studied the thermal and mechanical response characteristics of our system using finite element numerical analysis (FEA; COMSOL Multiphysics). The simulations accounted for heat transfer, gas expansion, and membrane mechanics. Detailed descriptions of the experiments and simulation methods are in Supplementary Methods.

Mechanical characterizations

Force measurements were captured with a load cell (LSB200, Futek, USA) and a strain gauge amplifier (CSG110, Futek, USA) using a data acquisition unit. The sample rate was 10 kHz. The load cell was applied with a preload of 0.74 N to ensure stable measurement conditions. Surface displacement measurements, as reported in Fig. 3, were captured via a laser triangulation sensor (Microtrak II LTC-025-02, MTI Instruments, USA) at a sample rate of 100 kHz. Surface velocity measurements, as reported in Fig. 1F and fig. S20, were captured via a scanning laser Doppler vibrometer (V/9100 1, Ometron), and surface measurements for fig. S19 were captured via single-point laser Doppler vibrometer (PDV-100, Polytec), both at a sample rate of 5 kHz.

Perceptual experiments

All six perceptual experiments were performed using a 437-pixel display surface (7.5 cm by 7.5 cm), with a pixel pitch of 3.6 mm (pixel density, 7.7 cm^{-2}). To inhibit light leakage, the flexible membrane (EcoFlex 00-10) was dyed white (Silc Pig White, Smooth-On), and a sheet of gold leaf (~0.1 μm thick) was adhered to the base. Neither modification notably affected the membrane mechanical response. A black curtain occluded the display from participants' view during the experiment. Although we observed no stray light, participants wore laser safety glasses to avoid safety concerns.

All participants gave their written informed consent. The protocol was approved by the human subjects review board at the authors' institution (protocol number 13-22-0139). The same 10 participants (4 females and 6 males; age, 19 to 34 years) completed the sequence of six experiments without training. None reported health issues or ailments affecting touch sensation. One additional participant was unable to complete the perceptual tasks for personal reasons unrelated to the experiment or device. These data were excluded. Participants' hand dimensions were measured. Right index finger pad widths were between 1.4 and 2.0 cm (mean, 1.6 cm), and hand lengths were between 16.5 and 19.5 cm (mean, 18.3 cm). Participants wore noise-isolating circumaural headphones playing white noise to mask auditory cues during the experiment. For each experiment, participants' fingers were positioned as depicted in Fig. 4. For familiarization with the device and procedure, participants felt all stimuli before each experiment began. The participants were not informed that this was a familiarization phase, were not given any information about the stimuli, and were not given any feedback about behavioral responses that they supplied. The data collected during this phase were not used for analysis. Detailed descriptions of the design, method, protocol, and analyses used for each of the six perceptual experiments are reported in Supplementary Methods.

Statistical analysis

Data were analyzed using MATLAB R2023b (MathWorks Inc., Natick, MA). Error bars represent one SD. Statistical regression analyses were performed using the MATLAB Curve Fitting Toolbox 23.2. For the perceptual studies, the high response accuracies in experiments 1, 2, 3, 5, and 6 precluded additional statistical analysis. In perceptual experiment 4, for each P_{L}, a geometric mean was calculated from the response data of each participant. The geometric mean of the participant was then normalized by the grand mean across all power levels to produce a value $I(P_{\mathrm{L}}, k)$ representing perceived intensity at P_{L} for participant k (*45*).

Supplementary Materials

The PDF file includes:
Methods
Figs. S1 to S21
Tables S1 to S6
References (*46*–*75*)

Other Supplementary Material for this manuscript includes the following:
Movies S1 to S6
MDAR Reproducibility Checklist

REFERENCES AND NOTES

1. J. E. Colgate, M. A. Peshkin, "Haptic interface for vehicular touch screens" (Tech. Rep., Center for the Commercialization of Innovative Transportation Technologies, 2013).
2. C. Serafin, R. Heers, M. Tschirhart, C. Ullrich, C. Ramstein, User experience in the US and Germany of in-vehicle touch screens with integrated haptic and auditory feedback. *SAE Transactions* **116**, 357–364 (2007).
3. A. Ng, S. Brewster, "An evaluation of touch and pressure-based scrolling and haptic feedback for in-car touchscreens," in *Proceedings of the 9th International Conference on Automotive User Interfaces and Interactive Vehicular Applications* (Association for Computing Machinery, 2017), pp. 11–20.
4. F. Guimbretière, M. Stone, T. Winograd, "Fluid interaction with high-resolution wall-size displays," in *Proceedings of the 14th Annual ACM Symposium on User Interface Software and Technology* (Association for Computing Machinery, 2001), pp. 21–30.
5. K. L. Dempski, B. L. Harvey, "Touchable interactive walls: Opportunities and challenges," in *Entertainment Computing–ICEC 2005: 4th International Conference, Sanda, Japan, September 19–21, 2005, Proceedings*, vol. 3711 of *Lecture Notes in Computer Science*, F. Kishino, Y. Kitamura, H. Kato, N. Nagata, Eds. (Springer, 2005), pp. 192–202.
6. N. Matsushita, J. Rekimoto, "HoloWall: Designing a finger, hand, body, and object sensitive wall," in *Proceedings of the 10th Annual ACM Symposium on User Interface Software and Technology* (Association for Computing Machinery, 1997), pp. 209–210.
7. T. Watanabe, M. Kobayashi, S. Ono, K. Yokoyama, "Practical use of interactive tactile graphic display system at a school for the blind," in *Proceedings of the Fourth International Conference on Multimedia and Information and Communication Technologies in Education (m-ICTE)* (Formatex, 2006), pp. 1111–1115.
8. D. Cingel, C. Blackwell, S. Connell, A. M. Piper, "Augmenting children's tablet-based reading experiences with variable friction haptic feedback," in *Proceedings of the 14th International Conference on Interaction Design and Children* (Association for Computing Machinery, 2015), pp. 295–298.
9. D. Wang, K. Ohnishi, W. Xu, Multimodal haptic display for virtual reality: A survey. *IEEE Trans Ind Electron* **67**, 610–623 (2020).
10. H. Benko, C. Holz, M. Sinclair, E. Ofek, "Normaltouch and texturetouch: High-fidelity 3d haptic shape rendering on handheld virtual reality controllers," in *Proceedings of the 29th Annual Symposium on User Interface Software and Technology* (Association for Computing Machinery, 2016), pp. 717–728.
11. J. C. Craig, P. M. Evans, Vibrotactile masking and the persistence of tactual features. *Percept. Psychophys.* **42**, 309–317 (1987).
12. C. Sherrick, "Vibrotactile pattern perception," in *The Psychology of Touch*, M. A. Heller, W. Schiff, Eds. (Taylor and Francis, 1991), pp. 239–261.
13. T. A. Kern, C. Hatzfeld, A. Abbasimoshaei, *Engineering Haptic Devices* (Springer Nature, 2023).
14. L. Jones, S. Lederman, *Human Hand Function* (Oxford Univ. Press, 2006).
15. D. Copeland, J. Finlay, Identification of the optimum resolution specification for a haptic graphic display. *Interact. Comput.* **22**, 98–106 (2010).
16. E. Leroy, R. Hinchet, H. Shea, Multimode hydraulically amplified electrostatic actuators for wearable haptics. *Adv. Mater.* **32**, e2002564 (2020).
17. G. Grasso, S. Rosset, H. Shea, Fully 3D-printed, stretchable, and conformable haptic interfaces. *Adv. Funct. Mater.* **33**, 2213821 (2023).
18. C. Shultz, C. Harrison, "Flat panel haptics: Embedded electroosmotic pumps for scalable shape displays," in *Proceedings of the 2023 CHI Conference on Human Factors in Computing Systems*, CHI '23 (Association for Computing Machinery, 2023), pp. 1–16.
19. J. Streque, A. Talbi, P. Pernod, V. Preobrazhensky, Pulse-driven magnetostatic micro-actuator array based on ultrasoft elastomeric membranes for active surface applications. *J. Micromech. Microeng.* **22**, 095020 (2012).
20. R. Wood, E. Steltz, R. Fearing, Optimal energy density piezoelectric bending actuators. *Sens. Actuators A Phys.* **119**, 476–488 (2005).
21. R. H. Heisser, C. A. Aubin, O. Peretz, N. Kincaid, H. S. An, E. M. Fisher, S. Sobhani, P. Pepiot, A. D. Gat, R. F. Shepherd, Valveless microliter combustion for densely packed arrays of powerful soft actuators. *Proc. Natl. Acad. Sci. U.S.A.* **118**, e2106553118 (2021).
22. S. Biswas, Y. Visell, Emerging material technologies for haptics. *Adv. Mater. Technol.* **4**, 1900042 (2019).
23. W. Yang, J. Huang, R. Wang, W. Zhang, H. Liu, J. Xiao, A survey on tactile displays for visually impaired people. *IEEE Trans. Haptics* **14**, 712–721 (2021).
24. Vybronics Ltd., LRA Coin Vibration Motor, model VG0415001W-240H (2020). RA/1.
25. S. Choi, K. J. Kuchenbecker, Vibrotactile display: Perception, technology, and applications. *Proc. IEEE* **101**, 2093–2104 (2013).
26. I. Hwang, H. J. Kim, S. Mun, S. Yun, T. J. Kang, A light-driven vibrotactile actuator with a polymer bimorph film for localized haptic rendering. *ACS Appl. Mater. Interfaces* **13**, 6597–6605 (2021).
27. N. Torras, K. E. Zinoviev, C. J. Camargo, E. M. Campo, H. Campanella, J. Esteve, J. E. Marshall, E. M. Terentjev, M. Omastová, I. Krupa, P. Teplický, B. Mamojka, P. Bruns, B. Roeder, M. Vallribera, R. Malet, S. Zuffanelli, V. Soler, J. Roig, N. Walker, D. Wenn, F. Vossen, F. M. H. Crompvoets, Tactile device based on opto-mechanical actuation of liquid crystal elastomers. *Sens. Actuators A Phys.* **208**, 104–112 (2014).
28. C. J. Camargo, H. Campanella, J. E. Marshall, N. Torras, K. Zinoviev, E. M. Terentjev, J. Esteve, Batch fabrication of optical actuators using nanotube–elastomer composites towards refreshable braille displays. *J. Micromech. Microeng.* **22**, 075009 (2012).
29. T. Hiraki, K. Nakahara, K. Narumi, R. Niiyama, N. Kida, N. Takamura, H. Okamoto, Y. Kawahara, Laser pouch motors: Selective and wireless activation of soft actuators by laser-powered liquid-to-gas phase change. *IEEE Robot. Autom. Lett.* **5**, 4180–4187 (2020).
30. A. G. Bell, On the production and reproduction of sound by light. *Am. J. Sci.* **s3-20**, 305–324 (1880).
31. J. Tyndall III, Action of an intermittent beam of radiant heat upon gaseous matter. *Proc. R. Soc. Lond.* **31**, 307–317 (1881).
32. W. C. Röntgen, Ueber Töne, welche durch intermittirende Bestrahlung eines Gases entstehen. *Ann. Phys.* **248**, 155–159 (1881).
33. M. Garbuny, M. J. Pechersky, "Optimization of engines operated remotely by laser power," in *Proceedings of the 2nd NASA Conference on Laser Energy Conversion* (NASA Ames Research Center, 1976), pp. 173–180.
34. H. Okamura, "On the efficiency of heat engines by pulsed laser," in *Proceedings of Optomechatronic Technologies 2008* [Society of Photo-Optical Instrumentation Engineers (SPIE), 2008], vol. 7266, pp. 70–76.
35. J. S. McKenzie, C. Clark, High sensitivity micromachined optical-to-fluid pressure converter for use in an optical actuation scheme. *J. Micromech. Microeng.* **2**, 245–249 (1992).
36. B. D. Hockaday, J. P. Waters, Direct optical-to-mechanical actuation. *Appl. Optics* **29**, 4629–4632 (1990).
37. J. O. Gurney, Photofluidic interface. *J. Dyn. Sys. Meas. Control.* **106**, 90–97 (1984).
38. A. Rosencwaig, Photoacoustic spectroscopy of biological materials. *Science* **181**, 657–658 (1973).
39. R. B. Peterson, "Micro thermal engines: Is there any room at the bottom?," in *ASME International Mechanical Engineering Congress and Exposition* (American Society of Mechanical Engineers, 1999), vol. 26683, pp. 81–88.
40. S. P. Burugupally, L. Weiss, Power generation via small length scale thermo-mechanical systems: Current status and challenges, a review. *Energies* **11**, 2253 (2018).
41. I. Sher, D. Levinzon-Sher, E. Sher, Miniaturization limitations of hcci internal combustion engines. *Appl. Therm. Eng.* **29**, 400–411 (2009).

42. R. T. Verrillo, Vibrotactile thresholds measured at the finger. *Percept. Psychophys.* **9**, 329–330 (1971).
43. M. Cellis, R. Pool, Two-point discrimination distances in the normal hand and forearm. *Plast. Reconstr. Surg.* **59**, 57–63 (1977).
44. P. Somers, A. Münchinger, S. Maruo, C. Moser, X. Xu, M. Wegener, The physics of 3D printing with light. *Nat. Rev. Phys.* **6**, 99–113 (2024).
45. L. A. Jones, H. Z. Tan, Application of psychophysical techniques to haptic research. *EEE Trans. Haptics* **6**, 268–284 (2013).
46. "Pyrolytic graphite sheet evolves: New twists on this thermally conductive material expand applications" (Tech. Rep., Panasonic Industrial Devices Sales Company of America, 2024).
47. D. Zhao, X. Qian, X. Gu, S. A. Jajja, R. Yang, Measurement techniques for thermal conductivity and interfacial thermal conductance of bulk and thin film materials. *J. Electron. Packag.* **138**, 040802 (2016).
48. M. R. Null, W. W. Lozier, A. W. Moore, Thermal diffusivity and thermal conductivity of pyrolytic graphite from 300 to 2700°K. *Carbon* **11**, 81–87 (1973).
49. L. Marechal, P. Balland, L. Lindenroth, F. Petrou, C. Kontovounisios, F. Bello, Toward a common framework and database of materials for soft robotics. *Soft Robot.* **8**, 284–297 (2021).
50. T. D. Bennett, *Transport by Advection and Diffusion: Momentum, Heat, and Mass Transfer* (Wiley, 2012).
51. A. Butland, R. Maddison, The specific heat of graphite: An evaluation of measurements. *J. Nucl. Mater.* **49**, 45–56 (1973).
52. C. A. Aubin, R. H. Heisser, O. Peretz, J. Timko, J. Lo, E. F. Helbling, S. Sobhani, A. D. Gat, R. F. Shepherd, Powerful, soft combustion actuators for insect-scale robots. *Science* **381**, 1212–1217 (2023).
53. International Organization for Standardization (ISO), *ISO 2631-2:2003 Mechanical Vibration and Shock — Evaluation of Human Exposure to Whole-Body Vibration, Part 2: Vibration in Buildings (1 Hz to 80 Hz)* (ISO, 2003); www.iso.org/standard/23012.html.
54. Y. Qiu, Z. Lu, Q. Pei, Refreshable tactile display based on a bistable electroactive polymer and a stretchable serpentine joule heating electrode. *ACS Appl. Mater. Interfaces* **10**, 24807–24815 (2018).
55. N. Besse, S. Rosset, J. J. Zarate, H. Shea, Flexible active skin: Large reconfigurable arrays of individually addressed shape memory polymer actuators. *Adv. Mater. Technol.* **2**, 1700102 (2017).
56. J. J. Zarate, O. Gudozhnik, A. S. Ruch, H. Shea, "Keep in touch: Portable haptic display with 192 high speed taxels," in *Proceedings of the 2017 CHI Conference Extended Abstracts on Human Factors in Computing Systems*, CHI EA '17 (Association for Computing Machinery, 2017), pp. 349–352.
57. A. K. Han, S. Ji, D. Wang, M. R. Cutkosky, Haptic surface display based on miniature dielectric fluid transducers. *IEEE Robot. Autom. Lett.* **5**, 4021–4027 (2020).
58. R. Velazquez, E. Pissaloux, M. Hafez, J. Szewczyk, "A low-cost highly-portable tactile display based on shape memory alloy micro-actuators," in *IEEE Symposium on Virtual Environments, Human-Computer Interfaces and Measurement Systems, 2005* (IEEE, 2005), 10.1109/VECIMS.2005.1567577.
59. E. Strasnick, S. Follmer, "Applications of switchable permanent magnetic actuators in shape change and tactile display," in *UIST '16 Adjunct: Adjunct Proceedings of the 29th Annual ACM Symposium on User Interface Software and Technology* (Association for Computing Machinery, 2016), pp. 123–125.
60. J. Kim, B.-K. Han, D. Pyo, S. Ryu, H. Kim, D.-S. Kwon, Braille display for portable device using flip-latch structured electromagnetic actuator. *IEEE Trans. Haptics* **13**, 59–65 (2020).
61. X. Wu, S.-H. Kim, H. Zhu, C.-H. Ji, M. G. Allen, A refreshable Braille cell based on pneumatic microbubble actuators. *J. Microelectromech. Syst.* **21**, 908–916 (2012).
62. Y. Kato, T. Sekitani, M. Takamiya, M. Doi, K. Asaka, T. Sakurai, T. Someya, Sheet-type Braille displays by integrating organic field-effect transistors and polymeric actuators. *IEEE Trans. Electron Dev.* **54**, 202–209 (2007).
63. I. M. Koo, K. Jung, J. C. Koo, J. D. Nam, Y. K. Lee, H. R. Choi, Development of soft-actuator-based wearable tactile display. *IEEE Trans. Robot.* **24**, 549–558 (2008).
64. S. Gallo, C. Son, H. J. Lee, H. Bleuler, I.-J. Cho, A flexible multimodal tactile display for delivering shape and material information. *Sens. Actuators A Phys.* **236**, 180–189 (2015).
65. V. Shen, T. Rae-Grant, J. Mullenbach, C. Harrison, C. Shultz, "Fluid reality: High-resolution, untethered haptic gloves using electroosmotic pump arrays," in *UIST '23: Proceedings of the 36th Annual ACM Symposium on User Interface Software and Technology* (Association for Computing Machinery, 2023).
66. E. Leroy, H. Shea, Hydraulically amplified electrostatic taxels (haxels) for full body haptics. *Adv. Mater. Technol.* **8**, 2300242 (2023).
67. Y. Wang, J. Liang, J. Yu, Y. Shan, X. Huang, W. Lin, Q. Pan, T. Zhang, Z. Zhang, Y. Gao, X. Yu, L. Wei, Z. Yang, Multiscale haptic interfaces for metaverse. *Device* **2**, 100326 (2024).
68. H. Phung, P. T. Hoang, C. T. Nguyen, T. N. Nguyen, H. Jung, U. Kim, H. R. Choi, "Interactive haptic display based on soft actuator and soft sensor," in *Proceedings of the 2017 IEEE/RSJ International Conference on Intelligent Robots and Systems (IROS)* (IEEE, 2017), pp. 886–891.
69. R. Uramune, H. Ishizuka, T. Hiraki, Y. Kawahara, S. Ikeda, O. Oshiro, HaPouch: A miniaturized, soft, and wearable haptic display device using a liquid-to-gas phase change actuator. *IEEE Access* **10**, 16830–16842 (2022).
70. C. W. Soule, N. Lazarus, Reconfigurable braille display with phase change locking. *Smart Mater. Struct.* **25**, 075040 (2016).
71. I. Hwang, S. Mun, J.-H. Youn, H. J. Kim, S. K. Park, M. Choi, T. J. Kang, Q. Pei, S. Yun, Height-renderable morphable tactile display enabled by programmable modulation of local stiffness in photothermally active polymer. *Nat. Commun.* **15**, 2554 (2024).
72. S.-Y. Jang, M. Cho, H. Kim, M. Choi, S. Mun, J.-H. Youn, J. Park, G. Hwang, I. Hwang, S. Yun, K.-U. Kyung, Dynamically reconfigurable shape-morphing and tactile display via hydraulically coupled mergeable and splittable PVC gel actuator. *Sci. Adv.* **10**, eadq2024 (2024).
73. J. Vaicekauskaite, P. Mazurek, S. Vudayagiri, A. L. Skov, Mapping the mechanical and electrical properties of commercial silicone elastomer formulations for stretchable transducers. *J. Mater. Chem. C* **8**, 1273–1279 (2020).
74. J. V. Chandar, S. Shanmugan, D. Mutharasu, M. Khairudin, A. A. Azlan, Polysiloxane-graphite composites as thermal interface material for light emitting diode application: A study on impact of graphite nanopowder on thermal and surface properties. *Polym.-Plast. Technol. Mater.* **59**, 106–115 (2020).
75. COMSOL Inc., *COMSOL Multiphysics Reference Manual*, version 6.1 (COMSOL Inc., 2022).

Acknowledgments: We gratefully acknowledge Y. Zhu, S. Adajian, B. Liao, and A. Sauret for assistance with characterization experiments. We thank N. Tummala for valuable comments. We acknowledge the Innovation Workshop and Microfluidics Lab in the UCSB California NanoSystems Institute, the UCSB MRSEC facility (NSF DMR 0520415), and the UCSB Nanofabrication facility, which were used in this research. **Funding**: No funding was received. **Author contributions:** M.L. and Y.V. designed research; M.L., D.G., G.R., and Y.V. performed research; M.L., D.G., G.R., V.K., E.H., and Y.V. analyzed data; M.L., G.R., E.H., and Y.V. wrote the paper. **Competing interests:** Authors M.L. and Y.V. are named inventors on a patent application (PCT number: PCT/US25/23182) related to this research. All other authors declare that they have no competing interests. **Data and materials availability:** All data needed to support the conclusions of this manuscript are included in the main text or Supplementary Materials. These data are also available on Zenodo (10.5281/zenodo.13948334).

Submitted 6 December 2024
Accepted 17 September 2025
Published 15 October 2025
10.1126/scirobotics.adv1383

Science Robotics

Tactile displays driven by projected light

Max Linnander, Dustin Goetz, Gregory Reardon, Vijay Kumar, Elliot Hawkes, and Yon Visell

Sci. Robot. **10** (107), eadv1383. DOI: 10.1126/scirobotics.adv1383

Science Robotics (ISSN 2470-9476) is published by the American Association for the Advancement of Science. 1200 New York Avenue NW, Washington, DC 20005. The title *Science Robotics* is a registered trademark of AAAS.